Evaluation on the Capability of Revealing Ocean Swells from *Sentinel-1A* Wave Spectra Measurements

XUAN WANG

College of Ocean Science and Engineering, Shanghai Maritime University, Shanghai, and College of Information Science and Engineering, Ocean University of China, and Laboratory for Regional Oceanography and Numerical Modeling, Qingdao National Laboratory for Marine Science and Technology, Qingdao, China

ROMAIN HUSSON

Collecte Localisation Satellites, Brest, France

HAOYU JIANG

College of Marine Science and Technology, China University of Geosciences, Wuhan, China

GE CHEN

College of Information Science and Engineering, Ocean University of China, and Laboratory for Regional Oceanography and Numerical Modeling, Qingdao National Laboratory for Marine Science and Technology, Qingdao, China

GUOPING GAO

College of Ocean Science and Engineering, Shanghai Maritime University, Shanghai, China

(Manuscript received 22 October 2019, in final form 7 May 2020)

ABSTRACT

Wave measurements retrieved by *Sentinel-1A* level-2 ocean (OCN) products are sensitive to swells other than wind seas, and are considered to provide a finer resolution of ocean swells. To assess the capability of swell retrieval globally, OCN products are validated against WAVEWATCH III (WW3) wave spectra for two available incidence angles [''wave mode'' (WV); WV1: 23°; WV2: 36°], focused on the integral wave parameters and most energetic wave system of *Sentinel-1A*. The wave parameter difference between *Sentinel-1A* and WW3 along antenna look angles for WV1 demonstrates the obvious impact of the nonlinearity influence in the azimuth direction, resulting in an unrealistically high wave height at the low wave frequency, and the spurious split of wave systems in the range direction, due to the vanishing of velocity bunching modulation. WV2 is less pronounced in these two aspects, but tends to shift wave energy to a higher wave frequency in the range direction. The inside discrepancy of wave energy has two noticeable features: the difference in peak wavelengths in the wave spectrum is positively clustered in the azimuth direction and negatively clustered in the range direction; some of the most energetic partitions derived from *Sentinel-1A* are difficult to assign to any wave systems in WW3. This phenomenon could be related to wind-wave coupling as the azimuth cutoff/WW3 peak wavelength is confined to a ratio below 0.5 for the negative difference between *Sentinel-1A* and WW3 peak wavelengths and the spectral distance of most energetic wave system in *Sentinel-1A* highly resembles ''swell pools.''

1. Introduction

Sentinel is a continuity mission that began after *ERS-1*, *ERS-2*, and *Envisat* ended in 2000, 2011, and 2012, respectively, with a finer spatial resolution, higher signal-to-noise, and broader image coverage. *Sentinel-1A* was launched on 3 April 2014 and is equipped with synthetic aperture radar (SAR), that routinely measures all-day accessible 2D swell spectra in open-ocean areas through a special image mode known as ''wave mode'' (WV). *Sentinel-1A* coverage is global with the exception of the northeast Atlantic. SAR, a unique satellite sensor that acquires

Corresponding author: G. Chen, gechen@ouc.edu.cn

DOI: 10.1175/JTECH-D-19-0060.1

global wave spectra, complements the coverage limitation of buoys and lack of directional information for altimeters. Because of the well-solved long waves, the implementation of SAR wave spectra in ocean studies has been focused on ocean swells. Unprecedented inclusion of global wave direction information has triggered new insights into wind and wave research, concerning tracking of swell origins (Holt et al. 1998; Collard et al. 2009), swell dissipation (Ardhuin et al. 2009; Stopa et al. 2016b), wave–current interaction (Liu et al. 1994) and crossing swell occurrence (Li 2016). SAR products have also become a common observation source for wave model assimilation (Abdalla et al. 2005) to improve hindcast performances (Stopa et al. 2016a).

Today, there is a good consensus on the SAR imaging mechanism of ocean surface waves. Analytical expressions describing the nonlinear ocean-to-SAR spectral transform constitute the basis for this understanding (Hasselmann and Hasselmann 1991), and the retrieved ocean spectra inevitably suffer from the azimuth cutoff caused by nonlinear velocity bunching displacement with satellite movement (Brüning et al. 1990; Hasselmann et al. 1985). Some SAR-to-wave retrieval methods that have a full view of the spectra need prior information from other sources. The Max Plank Institute for Meteorology (MPI) algorithm was first proposed and later developed by Hasselmann et al. (1996), who used the wave model spectrum as a first guess. The guessed wave spectrum is nonlinearly transformed into the SAR image spectrum, which is modified to minimize the cost function between the inverted SAR spectrum and the observed SAR spectrum. Krogstad et al. (1994) simplified the nonlinear mapping to quasi-linear mapping. Another inversion strategy, called the semiparametric retrieval algorithm (SPRA), adopts collocated scatterometer measurements to estimate wind seas and uses a quasi-linear relation to retrieve swells (Mastenbroek and De Valk 2000). Voorrips et al. (2001) compared MPI and SPRA against buoys and found that using the quasi-linear inversion algorithm in MPI deteriorates the wave model (WAM) spectrum, as nonlinearity introduces high-frequency waves to low-frequency regime that are misinterpreted as swells. Comparatively, SPRA does not resolve the short waves well, but produces better longer swells with 180° directional ambiguity. Cross-spectra of the image are used to resolve the 180° wave propagation ambiguities and remove the contribution from speckle noise bias in the image spectra (Engen and Johnsen 1995; Vachon and Raney 1991; Vachon and West 1992). Furthermore, an empirical approach known as CWAVE was proposed to estimate the integral wave parameters from the image orthogonal decomposition (Li et al. 2011; Schulz-Stellenfleth et al. 2007). Stopa and Mouche (2017) downsized input parameters to the normalized radar cross section (NRCS; or σ_0), azimuth cutoff (λ_c), normalized variance (Nv), skewness, peak wavelength (PW), and peak wave direction (PWD) to derive H_s, which is also valid under high wind conditions.

For the *Sentinel-1A* level-2 ocean (OCN) product, the retrieval scheme philosophy is to avoid the use of any priori ocean wave spectra and to linearize the inverse problem. The wind seas contribution to the nonlinear part of the cross-spectra is first estimated and then removed from the observed cross-spectra. The remaining part, the quasi-linear contribution, can then be solved analytically (Chapron et al. 2001). The explicit description of the ocean wave spectrum algorithm applied by level-2 OCN products is documented online (ESA 2020). Compared with the former mission, *Sentinel-1A* provides two incidence angles (WV1: 23°; WV2: 36°) to transmit and receive microwave signals. The increase in incidence angle leads to a decreasing tilt effect and differences in radar parameters, such as the normalized radar cross section, normalized variance, signal-to-noise ratio, and azimuth cutoff, which are directly related to the retrieval of oceanic parameters. *ERS-1* is a previous mission that carries SAR sensors. By comparison between *ERS-1* SAR observations and wave model spectra, approximately 75% of ocean swells can be well resolved (Heimbach et al. 1998). Jiang et al. (2017) found that even for the archived data with good quality flags in the advanced synthetic aperture radar (ASAR) dataset, the first and second energetic partitions may still not be in accordance with WW3 spectra. Mouche et al.(2016) validated the significant wave height (SWH) and wave periods of *Sentinel-1A* level-2 OCN products with WW3 and buoy for a 1-month period, but assessment of wave distribution in global basins and inner spectrum is further required. SAR imaging is affected by wind and sea state and the capability of swell retrieval is therefore inferred to be geographically dependent. By comparison, independently derived *Sentinel-1A* level-2 OCN products and wave model spectra could be a good indication of global data quality.

This paper presents a statistical assessment of *Sentinel-1A* level-2 OCN products with the reference to WW3 and buoy wave spectra, focusing on the energy distribution of wave spectrum in global geography. The data and the metrics used for comparisons and validation are shown in section 2. The detailed performances of geophysical parameters, including wave height, wavelength, wave direction, and wave system are examined at two different incidence angles in section 3. Efforts are made to find parameters to filter data outliers in the level-2

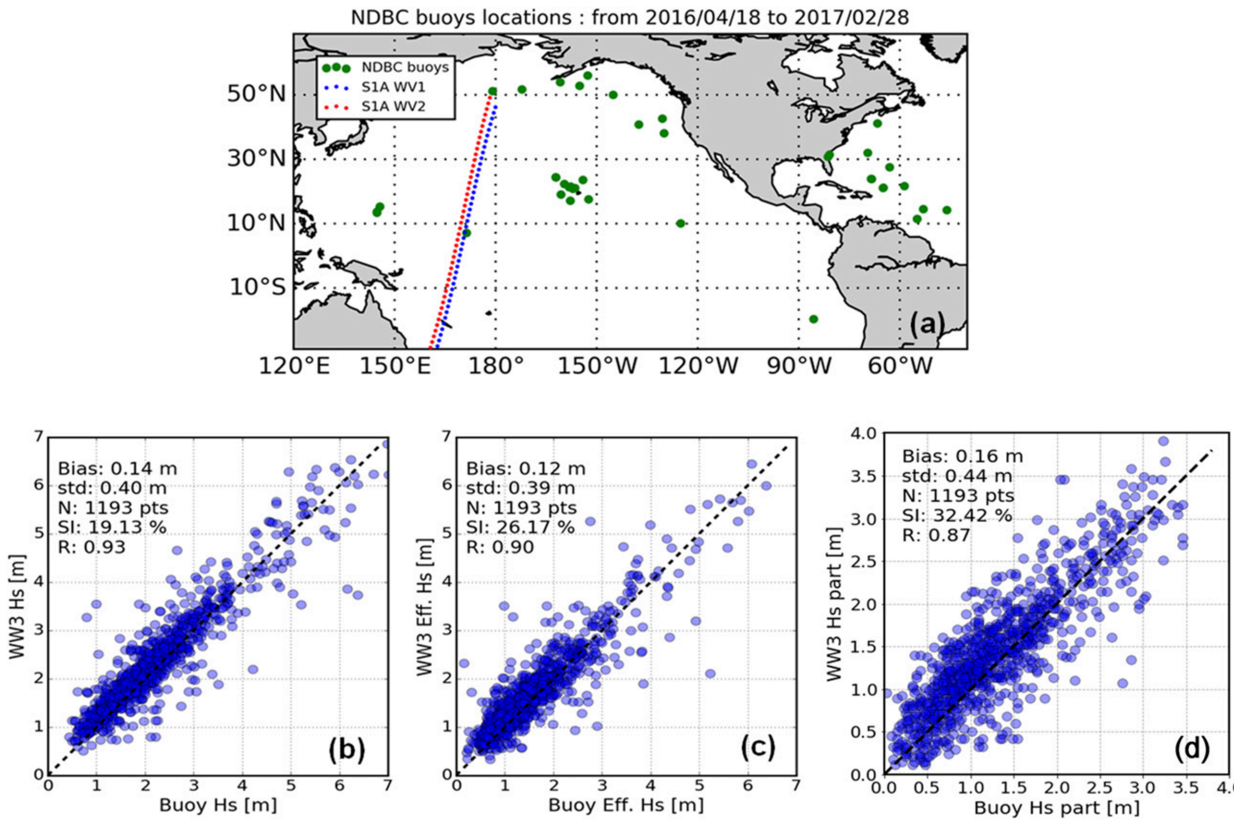

FIG. 1. (a) Location (green dots) of the in situ NDBC buoys with 2D ocean wave spectra used for this study. Illustration of the coverage for one descending pass obtained with *Sentinel-1A* from 1819 to 1849 UTC 17 May 2016. Blue and red dots represent WV1 and WV2, respectively, and indicate the location of acquisitions along the orbit. Comparison of SWH from the WW3 model and buoy observations for (b) total SWH, (c) effective SWH, and (d) partitioned SWH.

OCN products in section 4, and a discussion is presented in section 5.

2. Data and metrics

This section describes the data and metrics used for comparison and validation. *Sentinel-1A* SAR operates in wave mode only over open oceans where very few in situ measurements are available. Thus, our validation strategy relies on a combination of comparisons between SAR and the WW3 model. The SWH of the wave model is first validated with in situ buoys.

a. Sentinel-1A

A SAR *Sentinel-1A* is part of a 4 Earth observation satellite series for the European Copernicus environmental program. Sentinel-1 satellites carry C-band (5.405 GHz) SAR sensors operating in a sun-synchronous orbit at an altitude of 693 km with a repeat cycle of 175 orbits in 12 days. The satellites have a dedicated acquisition mode for ocean swell measurements. WV is single polarization only (HH or VV) and acquires alternatively in the near range (incidence angle: 23°; also called WV1) and far range (incidence angle: 36°; also called WV2). Wave mode acquires 20 km × 20 km vignettes every 100 km along the orbit, and vignettes on the same incidence angle are separated by 200 km. Swaths alternate incidence angles between the near range and far range, using VV as the default polarization mode. Figure 1 illustrates the coverage for one descending pass obtained with *Sentinel-1A* from 1819 to 1849 UTC 17 May 2016. Blue and red dots represent WV1 and WV2, respectively, and indicate the location of acquisitions along the orbit.

Level-0 data were processed by ESA Payload Data Ground Segment (PDGS) up to level-2 OCN. The main geophysical parameters are the ocean surface wind speed and wind direction, 2D wave spectrum and its associated partitions, as well as ocean surface radial velocities. The 2D wave spectrum is defined on a log–polar grid ($N_k = 60$, $N_f = 72$). Note that the grid resolution has increased by a factor of 2 with respect to *Envisat*/ASAR to benefit from direction and wavenumber resolutions achieved by Sentinel-1. The angular convention is such that 0° and 90° indicate swell propagation toward the north and east, respectively. Additional parameters regarding the image statistics or the ocean wave imaging mechanisms are also included, such as the normalized radar cross section, normalized variance, signal-to-noise ratio, azimuth cutoff, and spectral resolution of the ocean swell spectrum.

All results discussed hereinafter have been obtained using the level-2 OCN product processed by ESA PDGS from level 0. Launched on the 25 April 2016, *Sentinel-1B* is now in its commissioning phase; this mission is expected to have the same capacities as *Sentinel-1A*. VV is a default polarization mode for Sentinel-1, with over 90% of image data acquired under VV polarization. *Sentinel-1B* provides over 3 months of SAR images in HH polarization mode, from 17 March to 4 July 2017, which is a unique opportunity to compare these two different polarization modes. The modulation transfer function (MTF) was inaccurate for HH, as HH overestimated the wave height by approximately 0.60 m (0.30 m) higher than VV for WV1 (WV2). Therefore, in this study, we used data acquired from the VV polarization of *Sentinel-1A*, covering the whole ocean from 18 April 2016 to 28 February 2017.

b. Buoys

Most of the existing buoys are located in the Northern Hemisphere, primarily in Europe and North America. These buoys do not necessarily measure the full 2D ocean spectrum or even 1D ocean spectrum. Consequently, there are very few 2D ocean wave observations that can be directly used as reference data. Only the buoys in deep water were used to avoid the impact of the coasts. In particular, some buoys are located in the open ocean, such as Stratus (NDBC 32012). Collocations located within 200 km in space and 1 h in time, ocean swell measurements from *Envisat*/ASAR in wave mode have been validated against buoys by Collard et al. (2009). In this study, we rely on NDBC networks. Buoys locations are shown in Fig. 1. The directional wave spectrum is constructed by the archived first and second normalized polar coordinates from the Fourier coefficients using the methodology of maximum entropy method (MEM) (Lygre and Krogstad 1986).

c. WAVEWATCH III model

WW3 is a third-generation wave model developed by Delft University of Technology (Tolman and Chalikov 1996). WW3 solves the random phase spectral action density balance equation for wavenumber–direction spectra. The model used in this study relies on the development of the physical source term parameterizations proposed by Ardhuin et al. (2010) and Rascle and Ardhuin (2013) and validated by Stopa et al. (2016a). The model is operated by the Integrated Ocean Waves for Geophysical and other Applications (IOWAGA) group and uses a 0.5° global grid with 24 directions and 32 frequencies ranging from 0.0373 to 0.7159 Hz and are exponentially spaced with an increment of 1.1 Hz. The model is driven by 3-hourly winds and ice concentrations on the operational ECMWF product using a 0.125° global grid. Frequency–direction wave spectra are collocated in time and space using the closest point to match the *Sentinel-1A* acquisitions.

d. Wave partitioning

Hasselmann et al. (1996) introduced a methodology for 2D wave partitioning that uses watershed to separate different wave systems that originate from independent meteorological events; however, the threshold in merging partitions varies in other literature (Hanson and Phillips 2001; Portilla et al. 2009; Voorrips et al. 1997). In level-2 OCN products, spectral partitioning is applied to both the symmetric and antisymmetric parts of the ocean swell spectra in the polar grid after smoothing the spectra with a low pass filter. The spectral partitioning is recursive and applied to a given a priori number of partitions as five. A similar partitioning procedure was adopted in buoys and the WW3 wave spectrum to calculate the integral wave parameters as those given by level-2 OCN products. Before partitioning, the reference 2D wave spectrum was interpolated into the SAR grid and smoothed with a 3×3 convolution kernel. The total, effective and partitioned SWHs were computed from the 2D spectra for a comparison between the WW3 spectra and in situ buoys. The spectral resolution included in the *Sentinel-1A* level-2 OCN product was employed for effective SWH computation.

e. Metrics

The 2D ocean wave spectrum is defined as a function of the 2D density spectrum of wave heights $S(k, \theta)$ in wavenumber k and wave direction θ. At a given time and location, several wave systems can coexist. They are defined on a bounded domain in k or f after partitioning the 2D spectrum. In level-2 OCN products, each wave system (also called partitions, which can be up to five in the level-2 products) is described by three parameters estimated on the bounded domain: (i) SWH, (ii) PW, and (iii) PWD. These are the main validation parameters used here. Other parameters such as the spectral width of the peak can be defined from the 2D ocean wave spectrum; however, they are not included in the product and are not considered here. The total SWH is defined by

$$H_s = 4\sqrt{\int_f\int_\theta S(f,\theta)\,df\,d\theta} = 4\sqrt{\int_k\int_\theta S(k,\theta)k\,dk\,d\theta}, \quad (1)$$

where k is the wavenumber, θ is the direction, and $S(k, \theta)$ is the ocean wave height spectrum. Because of the imaging mechanism and the scatter displacement at the sea surface during the integration time, SAR cannot resolve the shortest wavelengths. This high-frequency limit is driven by the cutoff wavenumber (or cutoff wavelength). Taking this into account, the concept of effective SWH can be implemented and is defined as

$$H_{\mathrm{seff}} = 4\sqrt{\int_k\int_\theta S(k,\theta)\Gamma(k,\theta)k\,dk\,d\theta}. \quad (2)$$

The $\Gamma(k, \theta)$ function is usually defined by only considering the azimuth cutoff λ_c as follows:

$$\Gamma(k,\theta) = \begin{cases} 0, & \text{if} \quad k > k_c \\ 1, & \text{if} \quad k < k_c \end{cases}, \quad (3)$$

where k_c is the azimuth cutoff wavenumber. This threshold is estimated from the normalized azimuth profile of the estimated cross-covariance function in Sentinel products (ESA 2020) and is strongly related to sea state conditions. As defined in the quasi-linear theory, the cutoff can be written as

$$\lambda_c = \pi\frac{R}{V}\sqrt{\int_k \omega_k^2 S(k)\,dk}, \quad (4)$$

where R is the satellite range and V is the satellite velocity. The obtained mean values are 216 m for WV1 and 233 m for WV2. The dependency of the azimuth cutoff is approximately linear on $\sqrt{H_s}$ and wind speed U (Grieco et al. 2016). The effective SWH can also be computed by considering the spectral resolution parameter included in the product, detecting the shortest ocean wavelengths in terms of azimuth direction. This parameter is a vector of wavelengths equal to the number of directional bins

$$\lambda_c^{\mathrm{eff}} = \lambda_c \cos(\theta + \theta_{\mathrm{track}}) > \lambda_{\min}, \quad (5)$$

where $\lambda_{\min} = 2\pi/k_{\max} \approx 30$ m. In the range direction, the theoretical limit is given by the range bandwidth, and does not depend on the sea state. In the azimuth direction, it is the azimuth cutoff value. In this study, λ_c^{eff} is used to compute $\Gamma(k, \theta)$ and then obtain the effective SWH. PW and PWD are chosen as the wavelength and direction, respectively, where the maximum spectrum energy density is located. Effective partitioned PW and PWD can be computed from SAR and reference spectra partitions (i.e., WW3 and buoy) with wavenumber and direction intervals given by the partition domain defined in k and θ and limited by $\Gamma(k, \theta)$. They are defined as

$$S(k) = \int_\theta S_{R_p}(k,\theta)\Gamma(k,\theta)\,d\theta, \quad (6)$$

with $k_{\mathrm{peak}} = \arg_{\max}[S(k)]$, $\lambda_{\mathrm{peak}} = 2\pi/k_{\mathrm{peak}}$ for the effective partitioned PW, and

$$S(\theta) = \int_k S_{R_p}(k,\theta)\Gamma(k,\theta)\,dk, \quad (7)$$

with $\theta_{\mathrm{peak}} = \arg_{\max}[S(\theta)]$ for the effective partitioned PWD.

Scatterplots and statistical metrics are shown in Figs. 1b–d. The bias (standard deviation) is 0.14, 0.12, and 0.16 m (0.40, 0.39, and 0.44 m) for the total SWH, effective SWH, and partitioned SWH, respectively, between the WW3 model and buoy observations. A higher partitioned SWH value of 32.42% compared with a total SWH of 19.13% and an effective SWH of 26.17% is identified for the scatter index (SI). The correlation coefficients are 0.93 for the total SWH, 0.90 for the effective SWH and 0.87 for the partitioned SWH. There is good agreement between the WW3 and buoys. Therefore, WW3 output is used to assess the quality of *Sentinel-1A* level-2 OCN products in global basins.

3. Performances on wave parameters

a. Effective significant wave height

The effective SWH from *Sentinel-1A* versus WW3 is compared to obtain an overview of the performances on a global scale. The spectral resolution of the *Sentinel-1A* level-2 OCN product is used to compute the effective SWH from both *Sentinel-1A* and WW3 ocean wave spectra using Eqs. (2)–(4). WV1 and WV2 performances are analyzed separately. The bias between *Sentinel-1A* and WW3 is found at approximately 0 m for WV1 and 0.22 m for WV2 in Figs. 2a and 2b. Noticeably, the WV2 is more dispersed than WV1. For WV1 (WV2), the standard deviation is 0.43 m (0.51 m), SI is approximately 20% (25.9%) and the correlation coefficient is approximately 0.92 (0.89). When the effective SWH of WW3 is above 5 m, the SAR measured effective SWH shows only a minor increase in WV1 in Fig. 2a. It seems saturated for high sea states in WV1, and the effective SWH bias for two incidence modes in Figs. 2c and 2d shows an increase in wave height differences between WV1 and WV2 with increasing sea states. Figure 3 shows the spatial distribution of the differences between *Sentinel-1A* and WW3 for each WV with a cell size of 2° × 2°. For WV1, clear patterns are observed in

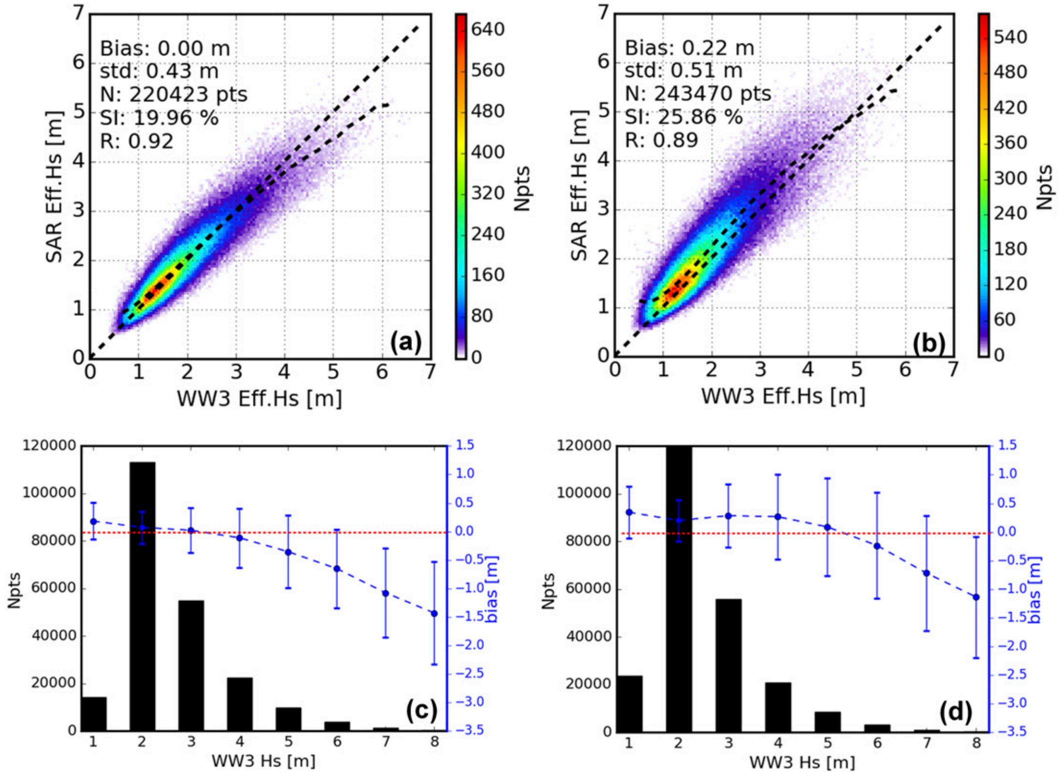

FIG. 2. (top) Scatterplots of collocated effective SWH of *Sentinel-1A* and WW3 for (a) WV1 and (b) WV2, and the black dashed line is the mean of effective SWH of *Sentinel-1A*. (bottom) Bias dependency of *Sentinel-1A* and WW3 effective SWH for (c) WV1 and (d) WV2. The number of collocations, bias, and standard deviations is calculated for each 1-m WW3 effective SWH bin from 0 to 8 m. Histograms show the number of collocations (left axis). Dotted lines represent the changes in the bias, with the error bar representing the standard deviation in each bin.

the performances. A significant and well-located underestimation of *Sentinel-1A* effective SWH exists in the high latitudes of the Southern Hemisphere, where storms are common and fiercer than those at the same latitudes in the Northern Hemisphere (Young et al. 2011). High sea states associated with high azimuth cutoff values are responsible for this underestimation, because the azimuth cutoff restricts the imaging of azimuth-traveling waves (Kerbaol et al. 1998; Stopa and Mouche 2017). An overestimation of effective SWH is observed in areas with low wind speeds; in particular, north of the Indian Ocean, east equatorial Pacific, along the California and central America coasts, and south of the Gulf of Guinea. In the extreme south of the Atlantic Ocean near Antarctica, a significant overestimation is also observed, corresponding to the existence of sea ice

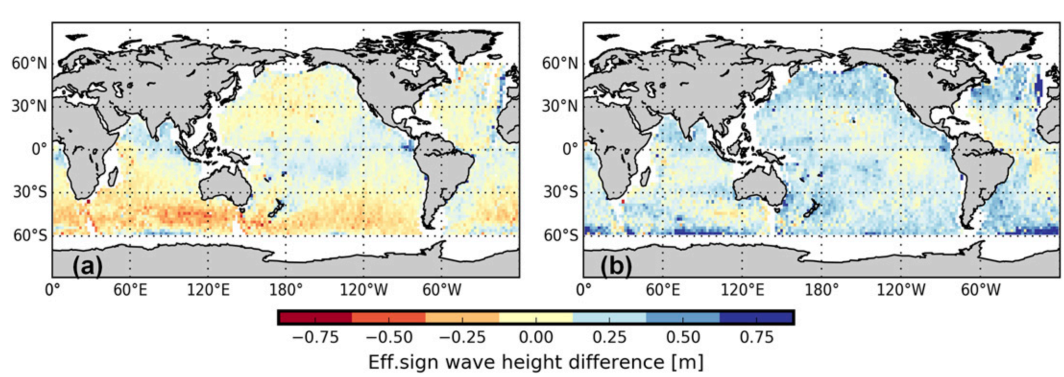

FIG. 3. Global map of the effective SWH difference between *Sentinel-1A* and WW3 for (a) WV1 and (b) WV2.

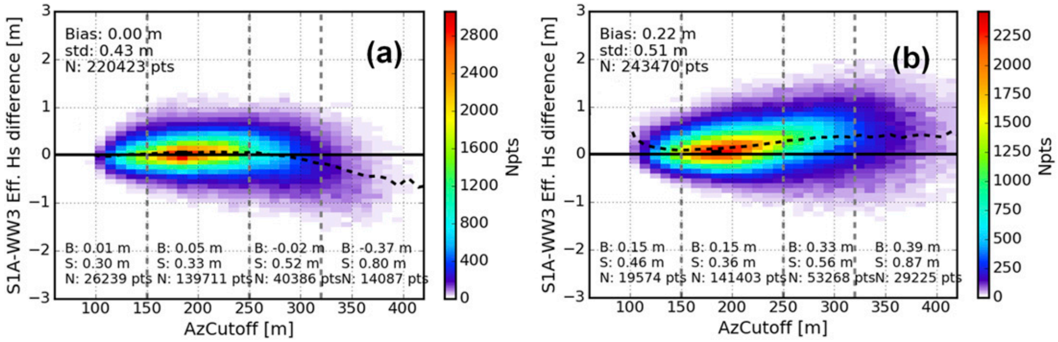

FIG. 4. Scatterplots of the effective SWH difference between *Sentinel-1A* and WW3 with respect to the azimuth cutoff for (a) WV1 and (b) WV2. The black dashed line is the mean of the effective SWH residual, and the gray dashed lines represent the azimuth cutoffs at 150, 250, and 320 m.

in the Southern Hemisphere. The spatial analysis of the results obtained with WV2 are less clear. Indeed, if we consider the bias of 0.22 m (the bias of Fig. 3b minus 0.22 m), we observed a similar but less pronounced pattern, except in the extreme southern latitudes of the Atlantic Ocean.

The direct analysis of the effective SWH difference with respect to the azimuth cutoff (correlated with wind speed and sea states), confirms the relationship between the WV1 and the WV2 performances and the geophysical parameters shown in the spatial analysis. In particular, for WV1, the analysis of the azimuth cutoff (see Fig. 4a) exhibits good performances for low azimuth cutoff (bias and standard deviation are approximately 0.05 and 0.33 m, respectively, when the azimuth cutoff is below 250 m and above 150 m) and a clear underestimation when the azimuth cutoff increases (bias and standard deviation are respectively approximately −0.37 and 0.80 m, respectively, when the azimuth cutoff is larger than 320 m). For WV2 (see Fig. 4b), there is a positive bias of 0.15 m and a standard deviation of 0.36 m when the azimuth cutoff is below 250 m and above 150 m. Bias and standard deviation rise to 0.39 and 0.87 m when the azimuth cutoff is between 320 and 400 m. When the azimuth cutoff is higher than 280 m, influenced by the saturation in WV1 shown in Fig. 2a, the effective SWHs of *Sentinel-1A* are underestimated during high wind conditions for WV1, but are overestimated for WV2.

b. *Peak wavelength and peak wave direction*

By finding where the spectral maximum energy is located, the definition of the PW and PWD can be proposed. The PW comparison between *Sentinel-1A* and WW3 has unexpectedly large discrepancies for both WV1 and WV2. Figures 5b and 5e show PW residuals (*Sentinel-1A* minus WW3) with respect to the PWD measured by *Sentinel-1A* relative to the antiantenna look angle. Here, 0° and 180° represent the up-waves and down-waves direction (i.e., aligned with the range direction). Additionally, 90° and 270° represent the cross-wave direction (i.e., aligned with the azimuth direction). For WV1, the positive PW differences between *Sentinel-1A* and WW3 are mostly located in the azimuth direction and are more concentrated than the negative differences. For WV2, the positive PW differences between *Sentinel-1A* and WW3 are less concentrated in the azimuth direction, and the negative differences show a distinct cluster in the range direction. The relationship between the PW residual and wind direction relative to the antiantenna look angle is given in Fig. 5a. The gathering of a large PW residual bias exists when wind is blown in the range direction, suggesting the existence of wind modulation.

Figures 5c and 5f show the PW residual (*Sentinel-1A* minus WW3) with respect to the PWD from WW3 relative to the antiantenna look angle. By comparing the different locations of distinct wavelength differences in the axis of PWD measured by *Sentinel-1A* and PWD modeled by WW3 relative to the antiantenna direction, those positive differences between *Sentinel-1A* and WW3 are found far from the azimuth direction in the WW3 spectrum. Motion-induced velocity bunching causes displacement of the pixel in the SAR images. Such a phenomenon implies a strong nonlinearity in the azimuth direction (Hasselmann and Hasselmann 1991; Hasselmann et al. 1996). As reported by Brüning et al. (1990), velocity bunching modulation significantly stretches the peak wavelength within 20° in the azimuth direction and rotates the spectral peak toward the range direction. As a result, the nonlinearity is not well resolved in *Sentinel-1A* products.

Furthermore, the unremoved nonlinearity in the level-2 OCN wave spectra is less severe in WV2 than in WV1, but the tendency to shift wave energy to a higher wave frequency in the range direction is more pronounced than WV1. In addition, the unmatched PWs

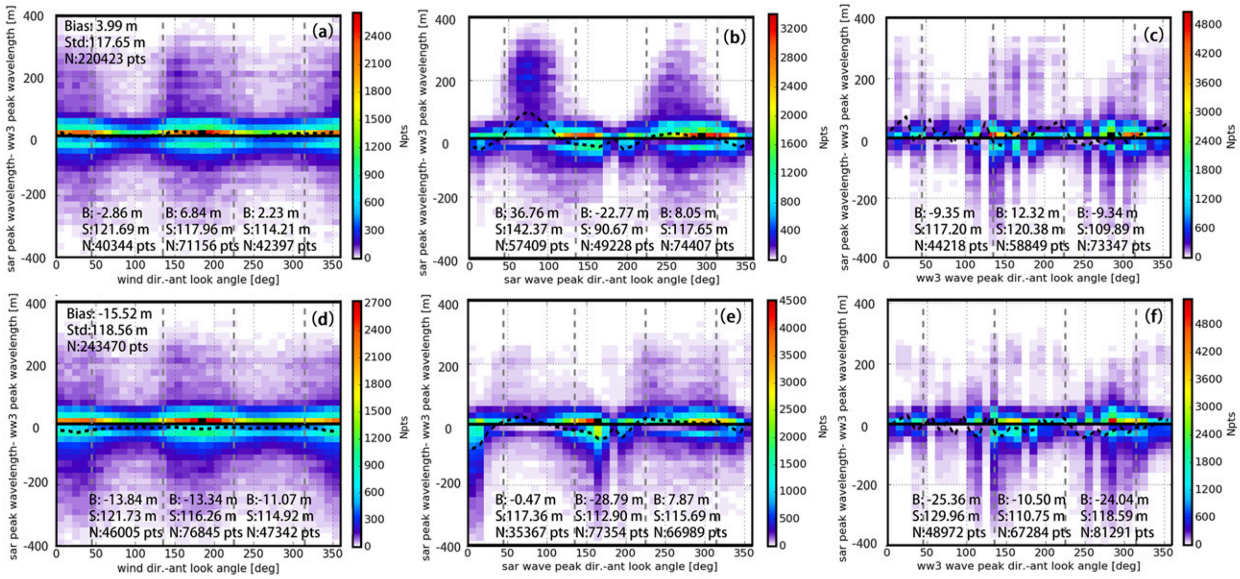

FIG. 5. (a)–(c) The PW difference between *Sentinel-1A* and WW3 for WV1 along the (a) wind direction relative to the antiantenna look, (b) *Sentinel-1A* PWD relative to the antiantenna look direction, and (c) WW3 PWD relative to the antiantenna look for WV1. The dashed line represents the binned average of the PW difference. (d)–(f) As in (a)–(c), but for WV2.

could also come from different relative energy distributions for *Sentinel-1A* and WW3. The global map of the PW difference between *Sentinel-1A* and WW3 is presented in Fig. 6 (which is very similar to the closest spectral distance in Fig. 8 between the *Sentinel-1A* and WW3 spectrum partitions defined in section 3b). The western Pacific is dominated by wind seas. As the inverted SAR image wave spectrum is appreciably limited to long ocean swells (i.e., the wavelength is longer than 200 m), the corresponding regions where *Sentinel-1A* PW is higher than WW3 are likely to suffer from cases where the most energetic wave systems of *Sentinel-1A* and WW3 do not match. The eastern Pacific is dominated by ocean swells, but the swells captured by SAR tend to rotate toward the range direction due to the effect of azimuth cutoff, exhibiting an underestimation of PW.

Compared with PW, it shows some wave signals retrieved by *Sentinel-1A* are unrealistically enforced in the azimuth direction or shifted to a higher frequency in the range direction. To further diagnose the enlargement of PW of Sentinel-1 in the azimuth direction and the reduction in the PW of Sentinel-1 in the range direction, the difference in the PWs between *Sentinel-1A* and WW3 along the azimuth cutoff/WW3 PW is plotted in Fig. 7. The azimuth cutoff/WW3 PW is mostly confined below 0.5 for the negative PW difference. The azimuth cutoff is positively related to sea state and surface wind conditions (Corcione et al. 2018), and waves whose PW is longer than 150 m can be defined as swells. Therefore,

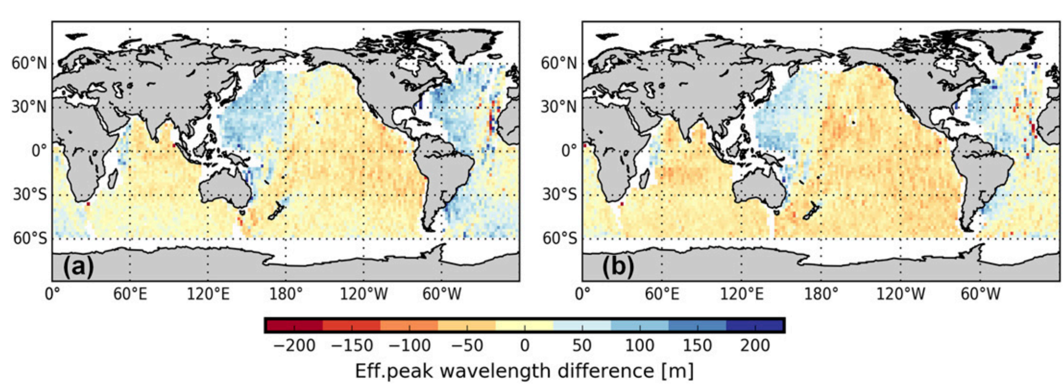

FIG. 6. Global map of the PW difference between *Sentinel-1A* and WW3 for (a) WV1 and (b) WV2.

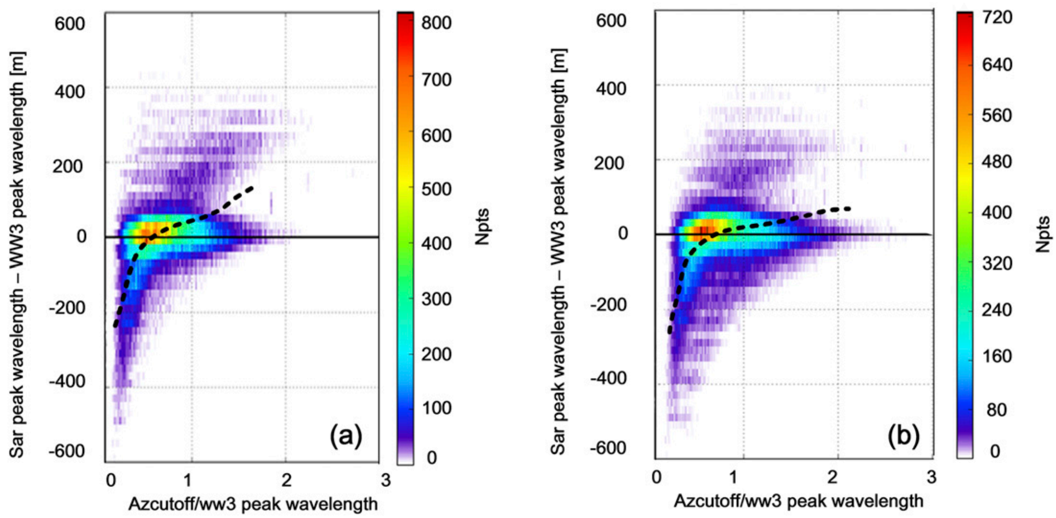

FIG. 7. Scatterplots of the PW difference between *Sentinel-1A* and WW3 with respect to the ratio of azimuth cutoff and WW3 PW for (a) WV1 and (b) WV2. The dashed line represents the binned average of the PW difference.

the parameter azimuth cutoff/WW3 PW is in relation to wind/swell, similar to the swell index proposed by Chen et al. (2002). The wind-dominated conditions overestimate the PW in the azimuth direction, and the swell-dominated conditions underestimate the PW in the range direction.

c. Wave system

The wave system performance analysis relies on the exact same data as the effective SWH. Here, only the wave system of the highest energy in the *Sentinel-1A* spectrum with WW3 is presented. The cross assignment between partitioned parameters from reference data and *Sentinel-1A* is performed using the following spectral distance as proposed by Husson (2012):

$$D = \frac{1}{q}\left[|D_1 - D_2| \bmod 360 + 2\frac{|T_1 - T_2|}{T_1 + T_2} r\right], \qquad (8)$$

where D_1 and D_2 represent the wave directions of SAR and WW3, respectively; T_1 and T_2 represent the wave periods of SAR and WW3, respectively; and $q = 30$ and $r = 250$. The 20° error in direction is equivalent to 8% errors in period, which is approximately the expected SAR wave measurement accuracies for wave direction and period. For each pair of *Sentinel-1A* ocean wave spectra and reference spectra, the two wave systems with the lowest spectral distance are cross assigned.

The spatial distribution of spectral distance is presented in Fig. 8. Small spectral distances as low as 0.8 (i.e., the spectra of *Sentinel-1A* and WW3 are well matched) are localized in areas known as "swell pools" (Semedo et al. 2011; Chen et al. 2002). In these pools, ocean swells dominate over wind seas and the distortion induced by nonlinearity is negligible (Chapron et al. 2001; Collard et al. 2009). Therefore, the quasi-linear retrieval algorithm functions better. The most energetic

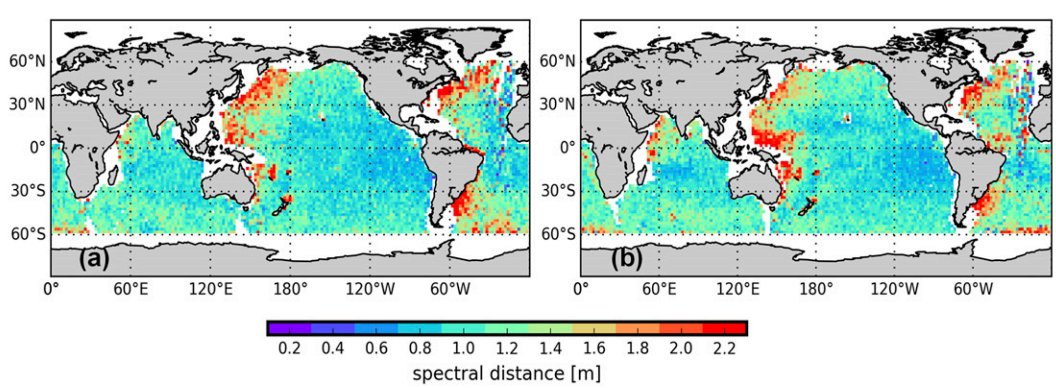

FIG. 8. Global map of the spectral distance between *Sentinel-1A* and WW3 for (a) WV1 and (b) WV2.

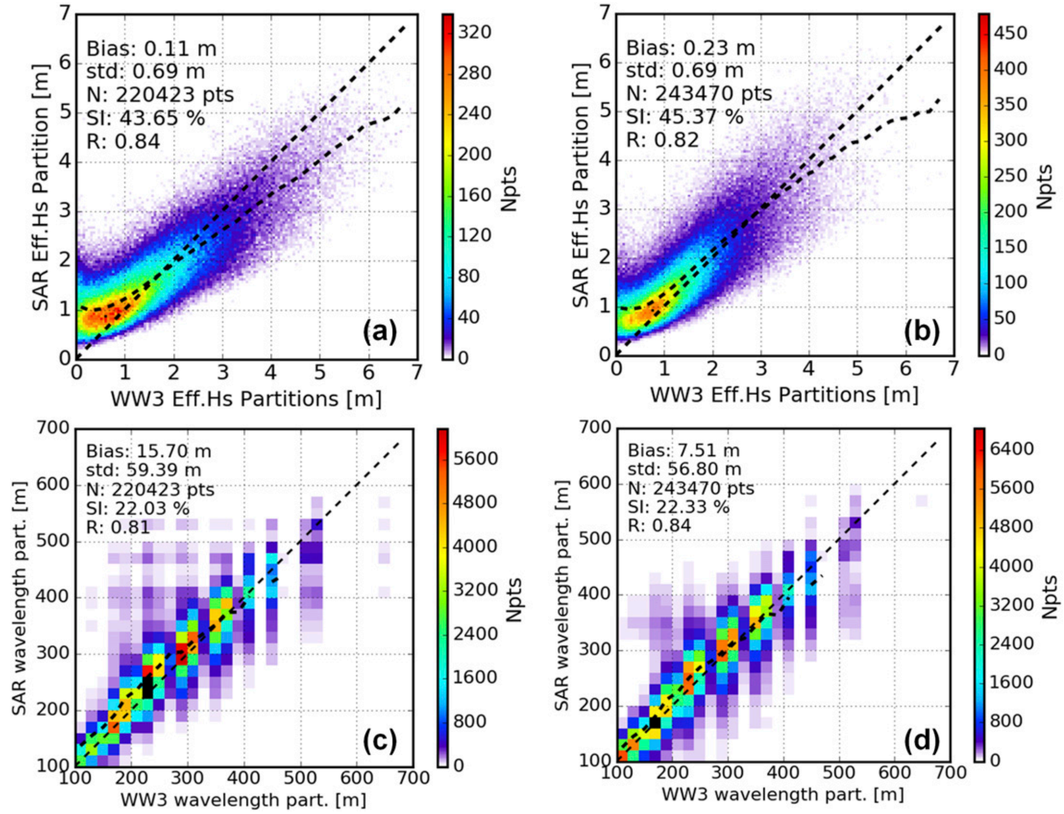

FIG. 9. Comparison of the partitioned integral parameters between *Sentinel-1A* and WW3: effective partitioned (a),(b) SWH and (c),(d) PW for (a),(c) WV1 and (b),(d) WV2. The dashed line represents the binned average of the effective partitioned SWH and PW.

partition in *Sentinel-1A* shows a positive bias of approximately 0.25 m (in Fig. 11), and the PW difference between *Sentinel-1A* and WW3 presents a negative bias of approximately 50 m (in Fig. 6). Large spectral distances (i.e., the spectra of *Sentinel-1A* and WW3 are poorly matched) are localized along the eastern coast of the continents. Many oceanic and atmospheric processes, such as precipitation, currents and ocean surface heat flux also display an easterly enforced spatial pattern (Chen et al. 2003; Kudryavtsev et al. 2014; Valdivieso et al. 2017). Geographical wave propagation could be misinterpreted by the low backscatter inferences from the existence of oceanic and atmospheric processes in inversion (Johannessen et al. 1991; Kudryavtsev et al. 2014; Nouguier et al. 2018; Quilfen et al. 1999), causing spurious wave traveling signals, which may be related to large spectral distances. The wave quality under different oceanic and atmospheric processes could be further analyzed with image classification for the WV mode (Wang et al. 2019). At present, the strong influence of oceanic and atmospheric processes can be categorized simply into large-scale features, and finding a method that will filter out poor measurements without the use of any prior information is critical for future research.

Figure 9 shows comparisons of the effective partitioned SWHs and PWs between wave systems, observed by *Sentinel-1A* and modeled by WW3, for both WV1 and WV2. Both WV1 and WV2 have a large bias when the effective partitioned SWH of WW3 is below 1 m. Effective partitioned PWs of *Sentinel-1A* are occasionally much longer than those of WW3. To avoid obvious outliers in the comparison, the effective partitioned PWD and PW difference are confined to 45° and 50 m, as shown in Fig. 10, which mitigates large bias in the low wave height of WW3. Biases are found at 0.05 and 0.22 m for WV1 and WV2, standard deviations are approximately 0.63 and 0.64 m, and correlations are approximately 0.87 and 0.83, respectively. The SI obtained with WV2 (40.4%) is larger than that obtained with WV1 (37.8%). Figure 11 gives the spatial distribution of the differences between *Sentinel-1A* and WW3 for each WV, showing a similar but larger-biased pattern as that in Fig. 3.

The wind direction relative to the antenna (Figs. 5a,d and 12a,c) presented no significant trend in bias or

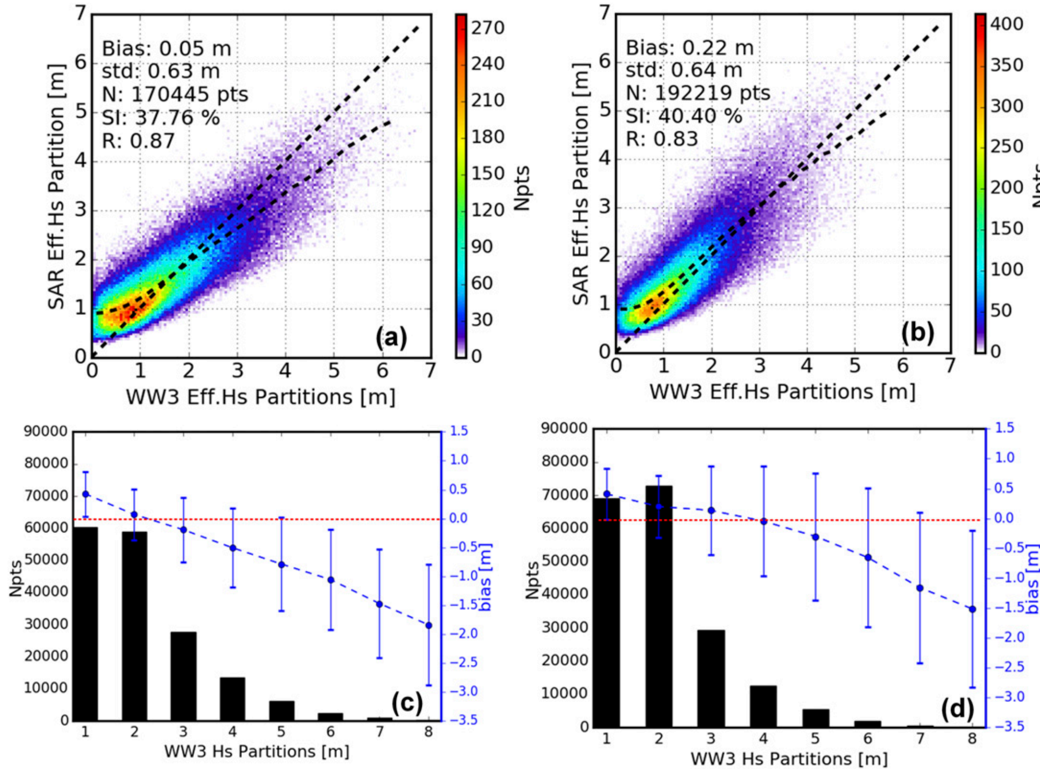

FIG. 10. (top) Scatterplots of collocated effective partitioned SWH of *Sentinel-1A* and WW3 for (a) WV1 and (b) WV2. The black dashed line is the mean of the effective partitioned SWH of *Sentinel-1A*. (bottom) Bias dependency of *Sentinel-1A* and WW3 effective partitioned SWH for (c) WV1 and (d) WV2. The number of collocations, bias, and standard deviations are calculated for each 1-m WW3 effective partitioned SWH bin from 0 to 8 m. Histograms show the number of collocations (left axis). Dotted lines represent the changes in the bias, with the error bar representing the standard deviation in each bin.

standard deviation. The performances obtained for the partitions significantly depended on the wave direction in Figs. 12b and 12d. The positive bias in the azimuth direction reflects the issues regarding the nonlinearity of the imaging mechanism. The standard deviation shows a clear increase and the bias turns negative for waves traveling around the range direction, which is associated with the split of the wave system and is known as the ‘‘double-peak phenomenon.’’ Brüning et al. (1988) showed that the SAR MTF has a strong lowest value near the range direction, where the occurrence of double peaks depends on the relative strength of velocity

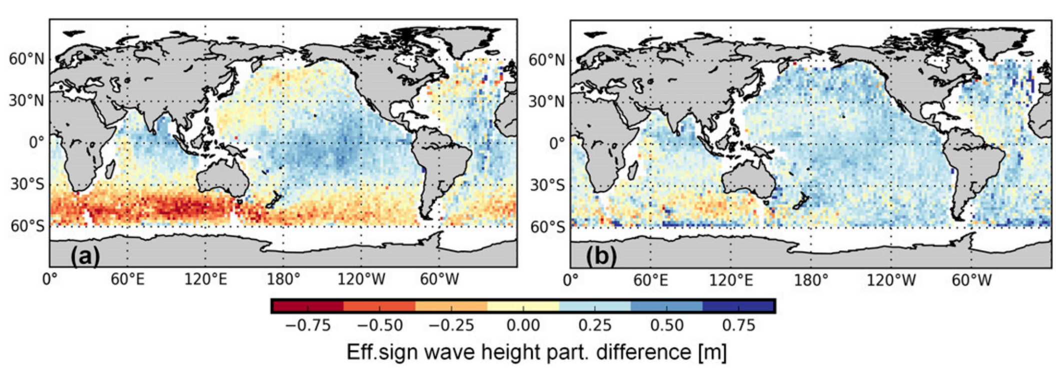

FIG. 11. Global map of the effective partitioned SWH difference between *Sentinel-1A* and WW3 for (a) WV1 and (b) WV2.

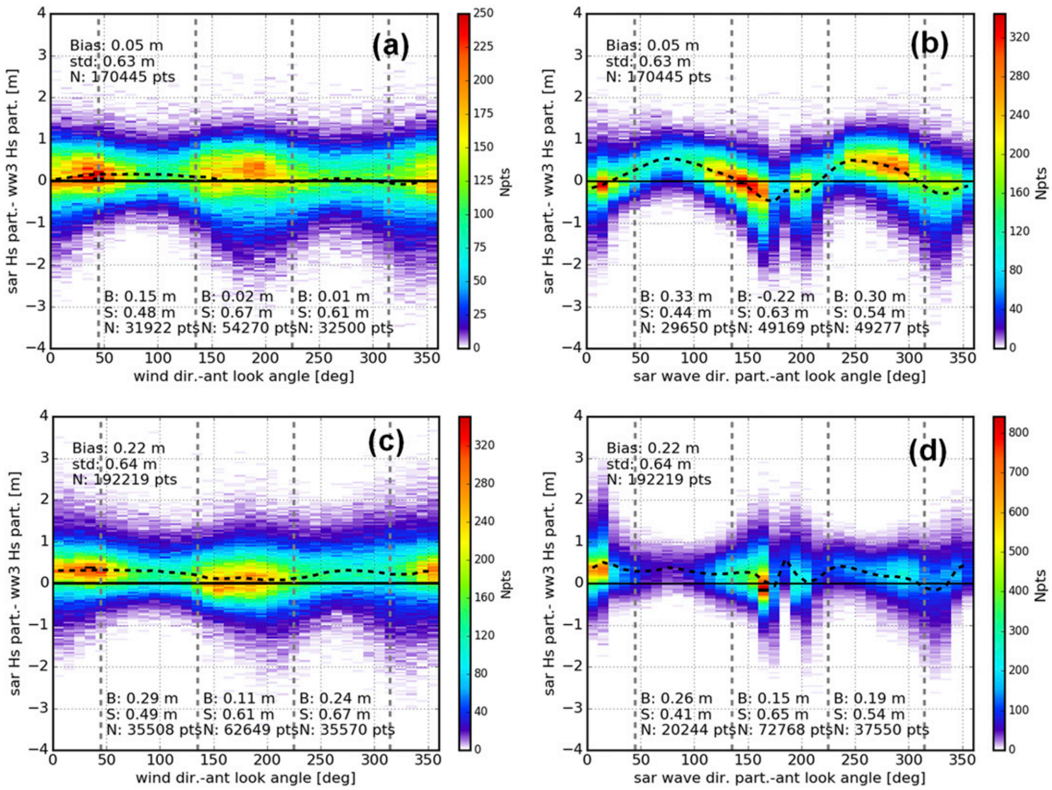

FIG. 12. Effective partitioned SWH difference between *Sentinel-1A* and WW3 for WV1 along (a) wind direction relative to the antiantenna look and (b) *Sentinel-1A* PWD relative to the antiantenna look direction. The dashed line represents the binned average of the effective partitioned SWH residual. (c),(d) As in (a) and (b), but for WV2.

bunching and cross-section modulation. As simulated by Brüning et al. (1990), the velocity bunching effects vanish in the range direction. The most energetic wave systems for WV2 tend to be located in the range direction compared with WV1. The symmetrical patterns in Fig. 5 and Fig. 12 along 180° comes from the ascending and descending passes, and two separate wind clusters originate from trade winds and westerlies. Because of the different track angles, this symmetry is not exactly mirrored.

4. Filtering ocean swell measurements

In addition to all the statistics given above, the wave direction ambiguity has also been checked. For WV1 (WV2), the percentage of the spectrum in which the partitions have a true partition is 95.5% (95.4%), have chosen a wrong wave direction is 9.0% (7.3%), have unremoved ambiguity is 33.3% (56.8%), and the percentage of spectrum that does not have a corresponding partition in WW3 is 51.8% (58.4%) (wavelength and wave direction differences are confined to 45° and 50 m, respectively). There are at most up to five partitions in one spectrum.

To avoid corruption from bad measurements in the *Sentinel-1A* level-2 OCN partitions, the data quality control has been considered: a wind speed threshold (normally 3 m s^{-1}) exists that generates enough Bragg waves to sustain σ_0. Waves become invisible in SAR images under low wind conditions due to the low signal-to-noise ratio (Clemente-Colón and Yan 2000). Stopa et al. (2015) computed the azimuth cutoff from the WW3 spectra, including the geometry effect of the wave propagation direction in relation to the radar line-of-sight and incidence angle [see their Eqs. (2)–(4)]. Stopa and Mouche (2017) further trained the WW3-derived azimuth cutoff with σ_0 and Nv provided by *Sentinel-1A* as input parameters. This empirical algorithm could provide a reference in comparison with the cutoff wavelength archived in level-2 OCN products with new estimation to filter the spectrum whose azimuth cutoff was wrongly estimated. The comparison indicates that the nonlinearity effect is not thoroughly removed and the image is contaminated by large-scale features, such as land, ice, wind streaks, oil slicks, and atmospheric fronts; therefore, it is necessary to filter partitions that are highly suspected to be spurious, or largely distorted.

The "repartition process" is performed on the image spectrum achieved in level-2 OCN products to recognize spurious partitions:

1) Smooth the image spectrum with a 3×3 convolution kernel.
2) Use the lowest closed contour line that encloses no more than three maximum extreme values in the image spectrum to define a noise level. If the image energy density is below this noise level, it will not be included in any partitions.
3) Repartition the image spectrum into different wave systems. The maximum extreme value of each partition is designated.
4) If a level-2 OCN partition includes a maximum extreme value of a new partition, or its image energy inside the new partition is larger than 50% of the image energy in the OCN partition, and the wavelength of the maximum extreme value for the intersected new partition is lower than 800 m, it will be kept.
5) Spurious partitions can be divided into unremoved nonlinearity that has no corresponding new partition or contamination from a large-scale feature, in which the corresponding new partitioned wavelength is larger than 800 m.

Taking all the above points into account, the filtering process eliminates the spectra with the following criteria:

1) The wind speed is lower than $3\,\mathrm{m\,s^{-1}}$.
2) The azimuth cutoff is 50 m away from the newly estimated azimuth.
3) The wave system is ambiguous, highly suspected of being a spurious wave system caused by nonlinearity or contaminated with large-scale features (the recognized spurious partitions after the repartition process).

The percentage of the spectrum whose spectral distance is larger than 2.5 is 7.4% (8.3%). The percentage of spectrum whose most energetic partition is ambiguous, a highly suspected spurious wave system caused by unremoved nonlinearity or large-scale features is 9.8% (12.6%). About 59.8% (61.2%) of the occurrence of large spectral distances can be explained by these filtering criteria. Finally, the statistical results of filtered effective partitioned SWH between *Sentinel-1A* and WW3 in Fig. 13 are comparable to those in Fig. 10 without the large bias in low WW3 wave height shown in Fig. 9, and the filtered dataset has a clear decrease in the data volume, where the PW difference is larger than 100 m.

5. Summary and conclusions

The comparison between *Sentinel-1A* and WW3 using nearly one year of data presents a low bias, low SI, and high correlation for effective SWH, comparable with the bias of 0.7 m for ASAR (Abdalla et al. 2006). The incidence angle WV2 measures the SWH higher than WV1, presenting a system bias of 0.22 m, and the wave height differences between WV1 and WV2 increase with increasing sea states. WV1 shows a low bias of 0.05 m and standard deviation of 0.35 m for an effective SWH difference in the range of 2–4 m and for an azimuth cutoff below 280 m. In regard to the most energetic partition paired with a corresponding wave system in WW3, the quality deteriorates. Spatially, the pattern of the most energetic effective partitioned SWH residuals resembles the effective SWH for each WV with an increase in bias. In the regions predominated by swells, the spectral distance is as low as 0.8, the most energetic partition in *Sentinel-1A* shows a positive bias of approximately 0.25 m, and the PW difference between *Sentinel-1A* and WW3 presents a negative bias of approximately 50 m.

The performances of the wave parameters' residuals and the wave direction relative to the antenna were analyzed in order to diagnose the energy distribution of the wave spectra. For WV1, the PW of *Sentinel-1A* was generally larger than that of WW3, and clustered in the azimuth direction; for WV2, the PW of *Sentinel-1A* was generally smaller than that of WW3, and clustered in the range direction. It is surprising that even the mean of the azimuth cutoff of WV2 was slightly higher than that of WV1, and the unremoved nonlinearity in wave spectra was not as severe as WV1. As illustrated by the PW and effective SWH difference between *Sentinel-1A* and WW3 along the relative PWD of *Sentinel-1A*, the wave energy measured by WV2 shifts toward a higher wave frequency in the range direction.

The disparity in wave energy between *Sentinel-1A* and WW3 is highly related to wind-wave coupling. The spatial pattern of the spectral distance and PW difference resembles "swell pools." Moreover, the large spectral distance also corresponds to regions where intense oceanic and atmospheric processes occur. A further step is necessary to examine the performance under different wind/swell conditions and oceanic and atmospheric processes (Wang et al. 2019), as the data quality for wave systems varies considerably with different environments. This should be particularly noted before applying *Sentinel-1A* wave measurements to further research.

Overall, wave systems derived from *Sentinel-1A* images are inevitably influenced by nonlinearity imbedded in imaging mechanisms and other oceanic or atmospheric contamination, which are not completely removed from OCN products at present and incur obvious discrepancies in paired wave systems from *Sentinel-1A* and WW3. Therefore, pretreatment to filter these

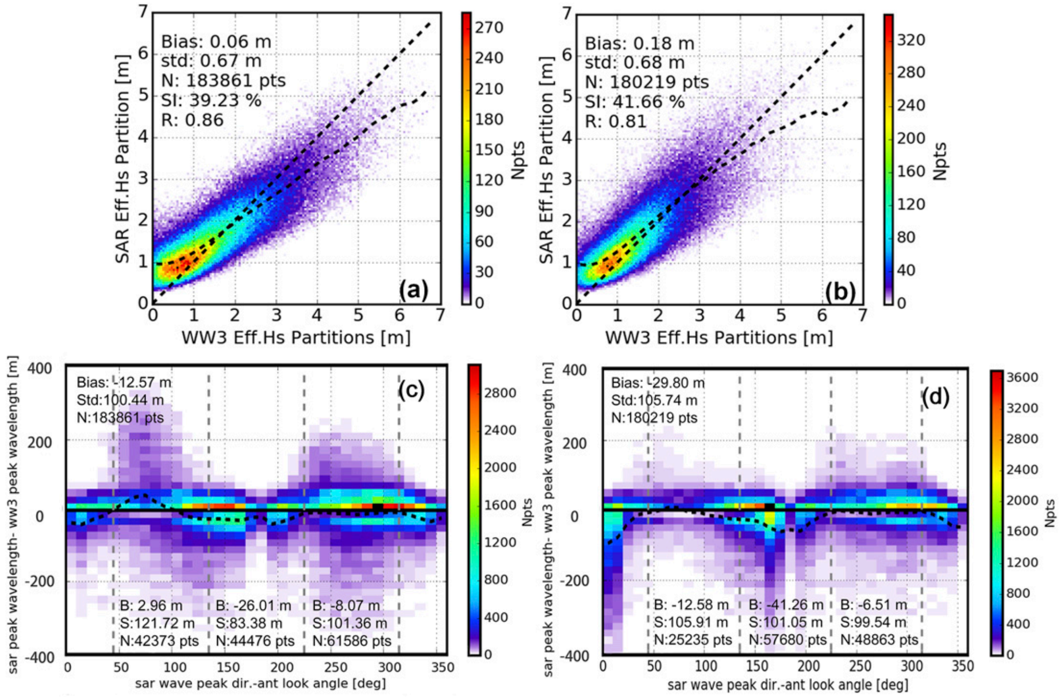

FIG. 13. (top) Scatterplots of filtered effective SWH between *Sentinel-1A* and WW3 for (a) WV1 and (b) WV2. The black dashed line is the mean of the effective partitioned SWH of *Sentinel-1A*. (bottom) Filtered PW difference between *Sentinel-1A* and WW3 along the *Sentinel-1A* PWD relative to the antiantenna look direction for (c) WV1 and (d) WV2. The dashed line represents the binned average of the PW difference.

wrongly inverted wave systems could serve as a better flag system for ocean swell spectra products. Over 50% of cases in which the PW and the partitioned SWH of Sentinel-1 are different from those of the WW3 model could be filtered with a repartition procedure. In a previous application of ASAR wave measurements, the spatial and temporal convergence of backward propagated wave systems was defined as a source of long traveling swells, which could also be used to flag the measured long waves that could not be associated with any sources (Mouche et al. 2016; Collard et al. 2009). Selecting SAR images that only contain wave signals is a solution to eliminate contaminated wave spectra, but this process is complex. As proposed by Wang et al. (2019), a deep convolutional neural network (CNN) can be employed to automatically classify SAR images into 10 geophysical categories: pure ocean waves, wind streaks, micro convective cells, rain cells, biological slicks, sea ice, icebergs, low wind areas, atmospheric fronts, and oceanic fronts. These labeled SAR images seem promising to improve the data quality by eliminating a wide range of oceanic and atmospheric conditions that contaminate the images.

Acknowledgments. This work was supported by the Strategic Priority Research Program of the Chinese Academy of Sciences (Grant XDA20060501 and XDA20060503), the National Natural Science Foundation of China (Grant 41331172), and National Key Research and Development Program of China (Grant 2016YFC1401008). We would also like to give thanks to Mouche Alexis for his support and guidance.

REFERENCES

Abdalla, S., J. R. Bidlot, and P. Janssen, 2005: Assimilation of ERS and Envisat wave data at ECMWF. *Envisat and ERS Symp.*, Salzburg, Austria, European Space Agency.

——, ——, and ——, 2006: Global validation and assimilation of Envisat ASAR wave mode spectra. *Proc. SeaSAR*, Frascati, Italy, European Space Agency, 8.1.

Ardhuin, F., B. Chapron, and F. Collard, 2009: Observation of swell dissipation across oceans. *Geophys. Res. Lett.*, **36**, L06607, https://doi.org/10.1029/2008GL037030.

——, and Coauthors, 2010: Semiempirical dissipation source functions for ocean waves. Part I: Definition, calibration, and validation. *J. Phys. Oceanogr.*, **40**, 1917–1941, https://doi.org/10.1175/2010JPO4324.1.

Brüning, C., W. Alpers, L. F. Zambresky, and D. G. Tilley, 1988: Validation of a synthetic aperture radar ocean wave imaging theory by the Shuttle Imaging Radar-B experiment over the North Sea. *J. Geophys. Res.*, **93**, 15 403–15 425, https://doi.org/10.1029/JC093iC12p15403.

——, ——, and K. Hasselmann, 1990: Monte-Carlo simulation studies of the nonlinear imaging of a two dimensional surface wave field by a synthetic aperture radar. *Int. J. Remote Sens.*, **11**, 1695–1727, https://doi.org/10.1080/01431169008955125.

Chapron, B., H. Johnsen, and R. Garello, 2001: Wave and wind retrieval from SAR images of the ocean. *Ann. Telecommun.*, **56**, 682–699, https://doi.org/10.1007/BF02995562.

Chen, G., B. Chapron, R. Ezraty, and D. Vandemark, 2002: A global view of swell and wind sea climate in the ocean by satellite altimeter and scatterometer. *J. Atmos. Oceanic Technol.*, **19**, 1849–1859, https://doi.org/10.1175/1520-0426(2002)019<1849:AGVOSA>2.0.CO;2.

——, J. Ma, C. Fang, and Y. Han, 2003: Global oceanic precipitation derived from TOPEX and TMR: Climatology and variability. *J. Climate*, **16**, 3888–3904, https://doi.org/10.1175/1520-0442(2003)016<3888:GOPDFT>2.0.CO;2.

Clemente-Colón, P., and X.-H. Yan, 2000: Low-backscatter ocean features in synthetic aperture radar imagery. *Johns Hopkins APL Tech. Dig.*, **21**, 116–121, https://www.jhuapl.edu/Content/techdigest/pdf/V21-N01/21-01-Clemente.pdf.

Collard, F., F. Ardhuin, and B. Chapron, 2009: Monitoring and analysis of ocean swell fields from space: New methods for routine observations. *J. Geophys. Res.*, **114**, C07023, https://doi.org/10.1029/2008JC005215.

Corcione, V., G. Grieco, M. Portabella, F. Nunziata, and M. Migliaccio, 2018: A novel azimuth cutoff implementation to retrieve sea surface wind speed from SAR imagery. *IEEE Trans. Geosci. Remote Sens.*, **57**, 3331–3340, https://doi.org/10.1109/TGRS.2018.2883364.

Engen, G., and H. Johnsen, 1995: SAR-ocean wave inversion using image cross spectra. *IEEE Trans. Geosci. Remote Sens.*, **33**, 1047–1056, https://doi.org/10.1109/36.406690.

ESA, 2020: Sentinel-1 level 2 ocean swell spectra processing. ESA, https://earth.esa.int/web/sentinel/technical-guides/sentinel-1-sar/products-algorithms/level-2-algorithms/ocean-swell-spectra-processing.

Grieco, G., W. Lin, M. Migliaccio, F. Nirchio, and M. Portabella, 2016: Dependency of the Sentinel-1 azimuth wavelength cut-off on significant wave height and wind speed. *Int. J. Remote Sens.*, **37**, 5086–5104, https://doi.org/10.1080/01431161.2016.1226525.

Hanson, J. L., and O. M. Phillips, 2001: Automated analysis of ocean surface directional wave spectra. *J. Atmos. Oceanic Technol.*, **18**, 277–293, https://doi.org/10.1175/1520-0426(2001)018<0277:AAOOSD>2.0.CO;2.

Hasselmann, K., and S. Hasselmann, 1991: On the nonlinear mapping of an ocean wave spectrum into a synthetic aperture radar image spectrum and its inversion. *J. Geophys. Res.*, **96**, 10 713–10 729, https://doi.org/10.1029/91JC00302.

——, R. K. Raney, W. J. Plant, W. Alpers, R. A. Shuchman, D. R. Lyzenga, C. L. Rufenach, and M. J. Tucker, 1985: Theory of synthetic aperture radar ocean imaging: A MARSEN view. *J. Geophys. Res.*, **90**, 4659–4686, https://doi.org/10.1029/JC090iC03p04659.

Hasselmann, S., C. Brüning, K. Hasselmann, and P. Heimbach, 1996: An improved algorithm for the retrieval of ocean wave spectra from synthetic aperture radar image spectra. *J. Geophys. Res.*, **101**, 16 615–16 629, https://doi.org/10.1029/96JC00798.

Heimbach, P., S. Hasselmann, and K. Hasselmann, 1998: Statistical analysis and intercomparison of WAM model data with global ERS-1 SAR wave mode spectral retrievals over 3 years. *J. Geophys. Res.*, **103**, 7931–7977, https://doi.org/10.1029/97JC03203.

Holt, B., A. K. Liu, D. W. Wang, A. Gnanadesikan, and H. S. Chen, 1998: Tracking storm-generated waves in the northeast Pacific Ocean with ERS-1 synthetic aperture radar imagery and buoys. *J. Geophys. Res.*, **103**, 7917–7929, https://doi.org/10.1029/97JC02567.

Husson, R., 2012: Development and validation of a global observation-based swell model using wave mode operating synthetic aperture radar. Ph.D. dissertation, Université de Bretagne Occidentale, 275 pp.

Jiang, H., A. Mouche, H. Wang, A. V. Babanin, B. Chapron, and G. Chen, 2017: Limitation of SAR quasi-linear inversion data on swell climate: An example of global crossing swells. *Remote Sens.*, **9**, 107, https://doi.org/10.3390/rs9020107.

Johannessen, J. A., R. A. Shuchman, O. M. Johannessen, K. L. Davidson, and D. R. Lyzenga, 1991: Synthetic aperture radar imaging of upper ocean circulation features and wind fronts. *J. Geophys. Res.*, **96**, 10 411–10 422, https://doi.org/10.1029/91JC00301.

Kerbaol, V., B. Chapron, and P. W. Vachon, 1998: Analysis of ERS-1/2 synthetic aperture radar wave mode imagettes. *J. Geophys. Res.*, **103**, 7833–7846, https://doi.org/10.1029/97JC01579.

Krogstad, H. E., O. Samset, and P. W. Vachon, 1994: Generalizations of the non-linear ocean-SAR transform and a simplified SAR inversion algorithm. *Atmos.–Ocean*, **32**, 61–82, https://doi.org/10.1080/07055900.1994.9649490.

Kudryavtsev, V., I. Kozlov, B. Chapron, and J. A. Johannessen, 2014: Quad-polarization SAR features of ocean currents. *J. Geophys. Res. Oceans*, **119**, 6046–6065, https://doi.org/10.1002/2014JC010173.

Li, X.-M., 2016: A new insight from space into swell propagation and crossing in the global oceans. *Geophys. Res. Lett.*, **43**, 5202–5209, https://doi.org/10.1002/2016GL068702.

——, S. Lehner, and T. Bruns, 2011: Ocean wave integral parameter measurements using Envisat ASAR wave mode data. *IEEE Trans. Geosci. Remote Sens.*, **49**, 155–174, https://doi.org/10.1109/TGRS.2010.2052364.

Liu, A. K., C. Y. Peng, and J. D. Schumacher, 1994: Wave-current interaction study in the Gulf of Alaska for detection of eddies by synthetic aperture radar. *J. Geophys. Res.*, **99**, 10 075–10 085, https://doi.org/10.1029/94JC00422.

Lygre, A., and H. E. Krogstad, 1986: Maximum entropy estimation of the directional distribution in ocean wave spectra. *J. Phys. Oceanogr.*, **16**, 2052–2060, https://doi.org/10.1175/1520-0485(1986)016<2052:MEEOTD>2.0.CO;2.

Mastenbroek, C., and C. F. De Valk, 2000: A semiparametric algorithm to retrieve ocean wave spectra from synthetic aperture radar. *J. Geophys. Res.*, **105**, 3497–3516, https://doi.org/10.1029/1999JC900282.

Mouche, A., H. Wang, R. Husson, G. Guitton, B. Chapron, and H. Li, 2016: 2D ocean waves spectra from space: A challenge for validation and synergetic use. *Proc. SPIE*, **9878**, 98780L, https://doi.org/10.1117/12.2227178.

Nouguier, F., B. Chapron, F. Collard, A. Mouche, N. Rascle, F. Ardhuin, and X. Wu, 2018: Sea surface kinematics from near-nadir radar measurements. *IEEE Trans. Geosci. Remote Sens.*, **56**, 6169–6179, https://doi.org/10.1109/TGRS.2018.2833200.

Portilla, J., F. J. Ocampo-Torres, and J. Monbaliu, 2009: Spectral partitioning and identification of wind sea and swell. *J. Atmos. Oceanic Technol.*, **26**, 107–122, https://doi.org/10.1175/2008JTECHO609.1.

Quilfen, Y., B. Chapron, A. Bentamy, J. Gourrion, T. El Fouhaily, and D. Vandemark, 1999: Global ERS 1 and 2 and NSCAT observations: Upwind/crosswind and upwind/downwind measurements. *J. Geophys. Res.*, **104**, 11 459–11 469, https://doi.org/10.1029/1998JC900113.

Rascle, N., and F. Ardhuin, 2013: A global wave parameter database for geophysical applications. Part II: Model validation with improved source term parameterization. *Ocean Modell.*, **70**, 174–188, https://doi.org/10.1016/j.ocemod.2012.12.001.

Schulz-Stellenfleth, J., T. König, and S. Lehner, 2007: An empirical approach for the retrieval of integral ocean wave parameters from synthetic aperture radar data. *J. Geophys. Res.*, **112**, C03019, https://doi.org/10.1029/2006JC003970.

Semedo, A., K. Sušelj, A. Rutgersson, and A. Sterl, 2011: A global view on the wind sea and swell climate and variability from ERA-40. *J. Climate*, **24**, 1461–1479, https://doi.org/10.1175/2010JCLI3718.1.

Stopa, J. E., and A. Mouche, 2017: Significant wave heights from Sentinel-1 SAR: Validation and applications. *J. Geophys. Res. Oceans*, **122**, 1827–1848, https://doi.org/10.1002/2016JC012364.

——, F. Ardhuin, B. Chapron, and F. Collard, 2015: Estimating wave orbital velocity through the azimuth cutoff from space-borne satellites. *J. Geophys. Res. Oceans*, **120**, 7616–7634, https://doi.org/10.1002/2015JC011275.

——, ——, A. Babanin, and S. Zieger, 2016a: Comparison and validation of physical wave parameterizations in spectral wave models. *Ocean Modell.*, **103**, 2–17, https://doi.org/10.1016/j.ocemod.2015.09.003.

——, ——, R. Husson, H. Jiang, B. Chapron, and F. Collard, 2016b: Swell dissipation from 10 years of Envisat advanced synthetic aperture radar in wave mode. *Geophys. Res. Lett.*, **43**, 3423–3430, https://doi.org/10.1002/2015GL067566.

Tolman, H. L., and D. V. Chalikov, 1996: Source terms in a third-generation wind wave model. *J. Phys. Oceanogr.*, **26**, 2497–2518, https://doi.org/10.1175/1520-0485(1996)026<2497:STIATG>2.0.CO;2.

Vachon, P. W., and R. K. Raney, 1991: Resolution of the ocean wave propagation direction in SAR imagery. *IEEE Trans. Geosci. Remote Sens.*, **29**, 105–112, https://doi.org/10.1109/36.103299.

——, and J. C. West, 1992: Spectral estimation techniques for multilook SAR images of ocean waves. *IEEE Trans. Geosci. Remote Sens.*, **30**, 568–577, https://doi.org/10.1109/36.142935.

Valdivieso, M., and Coauthors, 2017: An assessment of air–sea heat fluxes from ocean and coupled reanalyses. *Climate Dyn.*, **49**, 983–1008, https://doi.org/10.1007/s00382-015-2843-3.

Voorrips, A. C., V. K. Makin, and S. Hasselmann, 1997: Assimilation of wave spectra from pitch-and-roll buoys in a North Sea wave model. *J. Geophys. Res.*, **102**, 5829–5849, https://doi.org/10.1029/96JC03242.

——, C. Mastenbroek, and B. Hansen, 2001: Validation of two algorithms to retrieve ocean wave spectra from ERS synthetic aperture radar. *J. Geophys. Res.*, **106**, 16 825–16 840, https://doi.org/10.1029/1999JC000156.

Wang, C., and Coauthors, 2019: Classification of the global Sentinel-1 SAR vignettes for ocean surface process studies. *Remote Sens. Environ.*, **234**, 111457, https://doi.org/10.1016/j.rse.2019.111457.

Young, I. R., S. Zieger, and A. V. Babanin, 2011: Global trends in wind speed and wave height. *Science*, **332**, 451–455, https://doi.org/10.1126/science.1197219.